ADVANCED MATERIALS INTERFACES

www.advmatinterfaces.de

Hybrid InSe Nanosheets and MoS_2 Quantum Dots for High-Performance Broadband Photodetectors and Photovoltaic Cells

*Rajesh Kumar Ulaganathan, Kanchan Yadav, Raman Sankar, Fang Cheng Chou, and Yit-Tsong Chen**

Hybrid structures-based phototransistors are intensively studied recently to achieve high-performance optoelectronic devices. The hybridization of 2D materials and quantum dots (QDs) is one of the ideal platforms for photodetection applications with the merits of high detection sensitivity and wide wavelength coverage. The broadband absorption of a hybrid device stems from various absorbers with multiple bandgaps to create high photocurrent from an efficient exciton generation mechanism under illumination. Here, a new optoelectronic hybrid device of an indium selenide (InSe) nanosheets-based phototransistor is introduced decorated with molybdenum disulfide (MoS_2) QDs to possess the photoresponsivity (R_λ) of 9304 A W^{-1}, which is ≈10^3 times higher than R_λ ≈ 12.3 A W^{-1} of the previously reported InSe photodetector. The escalated R_λ of this hybrid photodetector is due to the additional injection of photoexcited charge carriers from MoS_2 QDs to the InSe phototransistor. Finally, the photovoltaic performance of this MoS_2/InSe hybrid device is investigated. The open-circuit voltage (V_{oc}) and short-circuit current density (J_{sc}) are determined to be 0.52 V and 15.6 mA cm^{-2}, respectively, rendering the photovoltaic efficiency of 3.03%. The development of this MoS_2/InSe hybrid phototransistor with high device performance and wide wavelength photodetection will bring a new type of optoelectronic applications in the future.

1. Introduction

To find new materials to substitute for conventional silicon (Si)-based technology that has been extensively used in logic circuits for decades, researchers have explored a wide plethora of materials to overcome the scaling limit of Si-based devices. Since the realization of device fabrications using single-layered graphene,[1,2] there has been great interest in 2D semiconductor materials with energy bandgaps to achieve high on-and-off current ratios and strong light absorption for electronic and optoelectronic utilizations.[3–6] The 2D layered materials are attractive building blocks in the modern electronic world with great potential to cope with the ever-changing demands of society. The novel layered structures have been explored for various applications, such as nanoscale electronics and optoelectronics, photodetectors and photovoltaics, energy storage, electrocatalysis, ultrasensitive sensors, and tissue engineering.[7–11] Compared with 0D and 1D materials, 2D layered crystals have excellent carrier mobility, large surface areas, and easy integration into the complex electronic circuitry, which provide advantages in the modern electronics industry.[12,13] Recent studies show that novel 2D crystals exhibit the high photoresponsivity, excellent external quantum efficiency (EQE), impressive specific detectivity, and a good response time in optoelectronic devices. These merits demonstrate that 2D layered crystals are promising candidates for high-performance electronics, optoelectronics, and energy-related applications.[14–17]

Dr. R. K. Ulaganathan, K. Yadav, Prof. Y.-T. Chen
Department of Chemistry
National Taiwan University
Taipei 10617, Taiwan
E-mail: ytcchem@ntu.edu.tw

Dr. R. K. Ulaganathan, K. Yadav, Prof. Y.-T. Chen
Institute of Atomic and Molecular Sciences
Academia Sinica
P.O. Box 23-166, Taipei 10617, Taiwan

Dr. R. K. Ulaganathan, Dr. R. Sankar, Prof. F. C. Chou
Center for Condensed Matter Sciences
National Taiwan University
Taipei 10617, Taiwan

The ORCID identification number(s) for the author(s) of this article can be found under https://doi.org/10.1002/admi.201801336.

DOI: 10.1002/admi.201801336

K. Yadav
Nanoscience and Nanotechnology Program
TIGP
Institute of Physics
Academia Sinica
Taipei 11529, Taiwan

Dr. R. Sankar
Institute of Physics
Academia Sinica
Nangang 11529, Taiwan

Prof. F. C. Chou
National Synchrotron Radiation Research Center
Hsinchu 30076, Taiwan

Prof. F. C. Chou
Taiwan Consortium of Emergent Crystalline Materials
Ministry of Science and Technology
Taipei 10622, Taiwan

To exploit innovative material characteristics and novel device designs, it is challenging for one material alone to achieve far-reaching applications in modern electronics. Nevertheless, the versatile hybrid devices of p–n, n–n, and p–p junctions have great potential for superior optoelectronic accomplishments.[18–20] Taking advantage of the ease of integration into the complex electronic circuitry, 2D crystals are suitable hybrid materials for developing a new generation of optoelectronics. Recently, hybrid phototransistors have been demonstrated to be of high detection sensitivity and wide wavelength response, which offer a very promising lead in the photodetector technology.[21–24] This burgeoning research gives plenty of exciting explorations of bringing distinctive nanomaterials together for versatile structural engineering and device architectures. In this study, we combined molybdenum disulfide (MoS_2) quantum dots (QDs) with indium selenide (InSe) nanosheets (denoted simply by MoS_2/InSe hereafter) to be used as the conducting channel of a hybrid device for high-performance broadband photodetectors and photovoltaic cells.

InSe, belonging to a family of group III–IV layered crystals, is arranged in a honeycomb lattice with four covalently bonded Se-In-In-Se planes, where the adjacent layers are weakly stacked together by van der Waals interaction with an interlayer distance of ≈0.8 nm. InSe is an n-type semiconductor with a direct bandgap of $E_g \approx 1.3$ eV (for bulk crystal)[25] and possesses excellent photoresponsive characteristics to offer great optoelectronic applications.[26,27] In our earlier study,[28] we demonstrated the photoresponsivity of an InSe field-effect transistor (InSe-FET) to be ≈12.3 A W^{-1}. In this report, we prepared a MoS_2/InSe-FET by incorporating InSe nanosheets with MoS_2 QDs, which were prepared from bulk MoS_2 crystal via a solvothermal method.[29] We enhanced the photoresponsivity of the MoS_2/InSe-FET to achieve $R_\lambda \approx 9304$ A W^{-1} at the 488 nm excitation, of which the photoresponsive improvement is $\approx 10^3$ times higher than our previous InSe-FET.[28] Like InSe, the MoS_2 layered crystal has attracted great attention because of its tunable optical bandgap,[30] efficient multiple exciton generation,[31] and good stability.[32]

Since the n–n type MoS_2/InSe heterostructure has a broad absorption profile,[33] we investigated the photoresponsive performance of this hybrid MoS_2/InSe-FET device from the visible to near-infrared regions. Upon photoexcitation, the junction interfaces and trap states of a MoS_2/InSe-FET could capture one type of charge carriers to delay the recombination of a free electron–hole pair in the wake of the photon absorption. As a result, other charge carriers with prolonged lifetimes can make several effective transits in the InSe channel between electrodes, leading to high photoconductive gain.[21,23,34] Moreover, the photoinduced electrons in MoS_2 QDs can be transferred to the InSe channel as additional charge carriers,[35] thus enhancing the photoresponsivity to 9304 A W^{-1}. Finally, we also conducted the photovoltaic measurements of this hybrid MoS_2/InSe-FET device to demonstrate the power conversion efficiency (PCE) of ≈3.03% with short-circuit current density (J_{sc}) of 15.6 mA cm^{-2} and open-circuit voltage (V_{oc}) of 0.52 V. Consequently, the hybrid MoS_2/InSe-FET system is found extremely efficient to achieve impressive broadband photodetection and photovoltaic efficiency, which are promising for cost-effective, yet highly responsive, optoelectronic manufactures.

2. Results and Discussion

InSe crystal was grown by the Bridgman technique with the detailed procedures described in the Experimental Section.[36] **Figure 1**a depicts the crystal structure of InSe with the stacking order via van der Waals interaction between the adjacent InSe layers, which can be exfoliated easily by mechanical exfoliation akin to graphene. In Figure 1b, the X-ray diffraction (XRD) spectrum of the as-synthesized InSe crystal shows the diffraction planes of (002), (004), (006), (008), and (0012) of a hexagonal structure with the lattice constants of $a = 4.005$ Å and $c = 16.64$ Å (Joint Committee on Powder Diffraction Standards (JCPDS)-34-1431). The presence of the In and Se elements in the as-grown InSe crystal was manifested by energy dispersive X-ray (EDX) analysis (Figure S1, Supporting Information). A field-emission scanning electron microcopy (FE-SEM) image of Figure 1c clearly shows the layered nature of InSe crystal. In Figure 1d, the single crystallinity of the exfoliated InSe crystal is further analyzed by selected-area electron diffraction (SAED), where the hexagonal structure with the Bragg spots of $<1\bar{1}00>$ and $<2\bar{1}\bar{1}0>$ are indicated.[28]

Figure 2a shows the schematic representation of MoS_2 QDs prepared from MoS_2 bulk crystal by a solvothermal method[29] with the detailed synthesis procedures presented in the Experimental Section. After the solvothermal reaction, while cooling the product to room temperature, the sample was settled down for a few hours to separate different sizes of MoS_2 QDs. It is interesting to note that MoS_2 bulk crystal (dark-black color) and MoS_2 QDs (light-yellow color) can be differentiated visually as shown in Figure 2b. The uniform size of MoS_2 QDs, ranging from 3 to 5 nm, was revealed by transmission electron microscopy (TEM) image (Figure 2c), thus demonstrating the successful fragmentation of the MoS_2 bulk structure via the serial sonication and solvothermal reactions. In Figure 2d, the SAED pattern of the as-prepared MoS_2 QDs indicates their polycrystalline structure. Moreover, the elemental compositions of Mo and S in the MoS_2 QDs, revealed by EDX analysis (Figure S2, Supporting Information), confirm the successful sample preparation. We also obtained the Raman spectra of MoS_2 QDs (blue trace) and MoS_2 bulk crystal (black trace) in Figure S3 in the Supporting Information, where the slight blueshift at 378 cm^{-1} (E^1_{2g}) and redshift at 404 cm^{-1} (A_{1g}) of MoS_2 QDs (blue line), due to the reduced number of layers from bulk crystal, confirm the presence of MoS_2 QDs.[37]

Figure 3 compares the electrical and optoelectronic properties of the FET devices fabricated by pristine InSe nanosheets alone and the hybrid MoS_2/InSe heterostructure, respectively. Figure 3a illustrates the schematic diagram of an InSe-FET, where multilayered InSe nanosheets were exfoliated by the scotch tape method, laid on a silicon wafer of a 300 nm thick SiO_2 oxidized layer, deposited with electrodes (Cr/Au = 5/70 nm in thickness) by evaporation via a shadow-mask technique. In Figure 3b, the thickness of the conducting InSe nanosheets of an InSe-FET (with its optical image shown in the upper inset) was determined to be ≈10 nm by atomic force microscopy (AFM, in the lower inset). Figure 3c illustrates the device architecture of a hybrid MoS_2/InSe-FET under photoresponsive investigation, where MoS_2 QDs were coated on an InSe-FET by physical adsorption. In the device fabrication, 5 mg mL^{-1} MoS_2 QDs

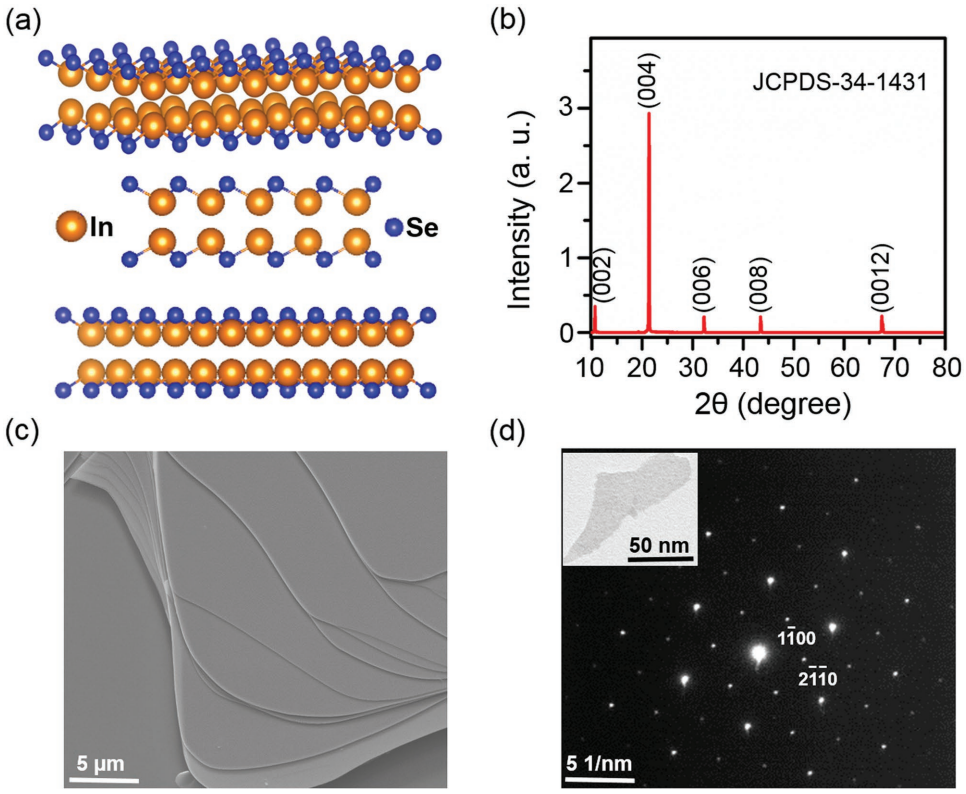

Figure 1. a) (Top) The 3D view and (bottom) profile view of the InSe crystalline structure with the orange and blue spheres representing the In and Se atoms, respectively. b) The XRD spectrum of the as-synthesized InSe crystal was observed and assigned. c) The layered nature of the InSe crystal is manifested by the observed SEM image. d) The SAED pattern of InSe nanosheets was identified to be a hexagonal single crystal. The inset shows a TEM image of the InSe nanosheets investigated.

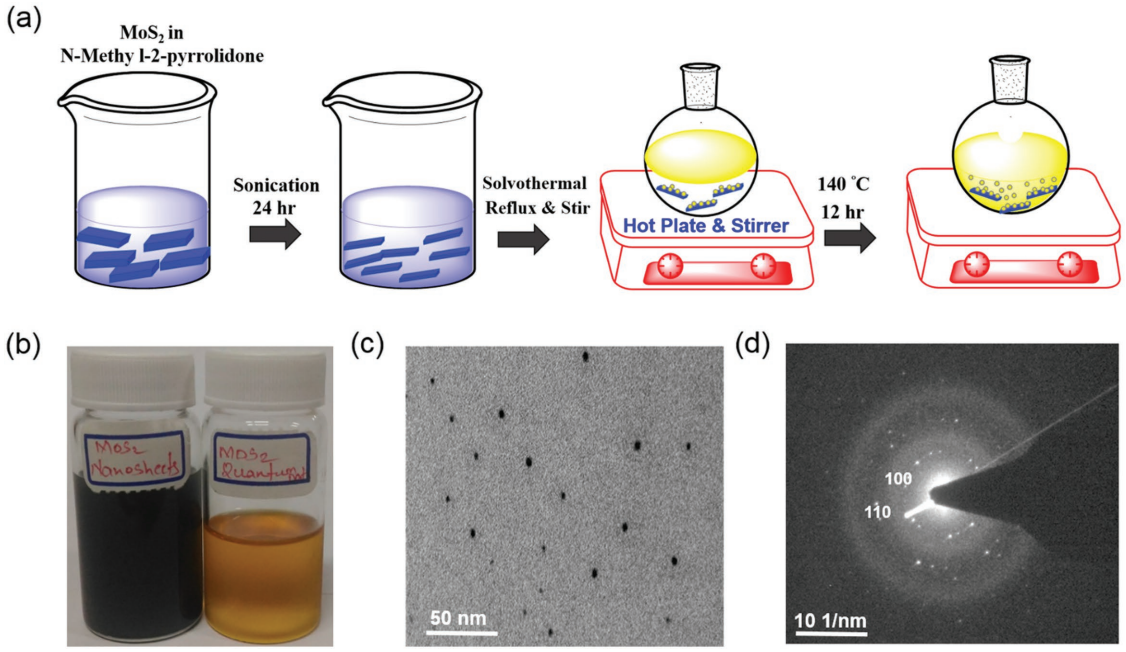

Figure 2. a) A schematic representation illustrates the preparation of MoS_2 QDs from MoS_2 bulk crystal. The MoS_2 bulk crystal was sonicated for 24 h in NMP, followed by solvothermal refluxing in the sonicated solution at 140 °C for 12 h to obtain MoS_2 QDs. b) A sharp color contrast between (left) dark-black MoS_2 nanosheets and (right) light-yellow MoS_2 QDs can be visualized to distinguish these two samples. c) A TEM image of the as-prepared MoS_2 QDs indicates the particle size of ≈3–5 nm. d) An SAED pattern of the as-prepared MoS_2 QDs reveals its polycrystalline structure.

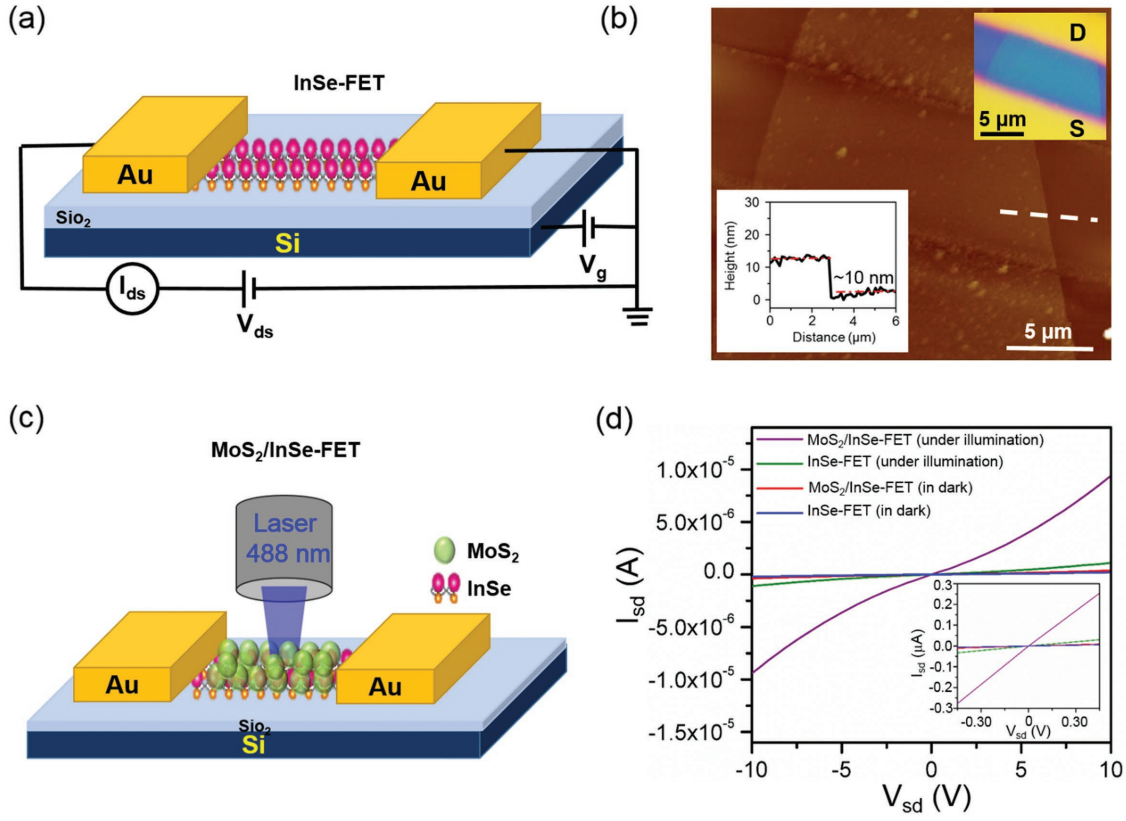

Figure 3. a) A schematic illustration of an InSe-FET device. b) The thickness of InSe nanosheets, which were used as the conducting channel of an InSe-FET, was determined by AFM. While the top inset represents the optical image of an InSe-FET device, the bottom inset shows the thickness of the conducting channel of InSe nanosheets to be ≈10 nm. c) A diagrammatic view of a hybrid MoS_2/InSe-FET device under photoresponsive measurements with laser excitation at 488 nm. d) The output curves (i.e., I_{sd}–V_{sd} plots) of an InSe-FET and a hybrid MoS_2/InSe-FET were measured separately in both dark and illuminative states. The inset shows a good contact between the InSe channel and electrodes.

were diluted in ethanol, spin coated onto the active channel area of an InSe-FET, and annealed at 180 °C for 30 min. The distribution of MoS_2 QDs on the channel area of InSe-FET was analyzed by both FE-SEM and EDX mappings, before and after the deposition of MoS_2 QDs. After MoS_2 QDs were deposited, the random distribution of MoS_2 QDs all over the InSe-FET is clearly seen in the SEM image (Figure S4, Supporting Information). Figure 3d shows the output curves (i.e., I_{sd}–V_{sd} plots) of an InSe-FET and a hybrid MoS_2/InSe-FET measured separately in both dark and illuminative states. In the inset of Figure 3d, we showed the symmetric characteristic of the MoS_2/InSe-FET device at the lower bias voltage to indicate the good contact between the channel and electrodes. Upon light illumination, the InSe-FET exhibits an apparent increase of the channel current (green line) in sharp contrast with the weak dark current measured in the dark state (blue line). This increase of the channel current is defined as the photocurrent (I_{ph}), where $I_{ph} = I_{light} - I_{dark}$ was calculated by deducting the current obtained in the dark (denoted by I_{dark}) from that measured with light exposure (represented by I_{light}). When illuminating the InSe-FET, the strong spectral absorption of InSe allows more charge carriers to be excited from the valence to conduction bands, resulting in greater charge carriers transporting to the external circuit and consequently driving higher current. By sensitizing the InSe-FET with MoS_2 QDs, the I_{ds}–V_{ds} measurement exhibits a greater enhancement in the photocurrent (purple line) of the MoS_2/InSe-FET. This observation suggests that photoexcited charge carriers exchanged actively between MoS_2 QDs and the InSe conducting channel, leading to efficient charge transfer at the MoS_2/InSe interface and resulting in enhanced photocurrent in the MoS_2/InSe-FET (also see the energy diagram in Figure 5b).[19,22] We also recorded the transfer curves (i.e., the source–drain current vs gate voltage, I_{ds}–V_g plots) of an InSe-FET and a hybrid MoS_2/InSe-FET by sweeping back-gate voltage from −20 to +80 V at V_{ds} = 1 V under both dark and illuminative (at λ = 488 nm) states (Figure S5, Supporting Information). Both devices exhibit n-type semiconductor characteristics and the photocurrent induced in the MoS_2/InSe-FET could be elevated ≈30 times higher than a bare InSe-FET.

Photoresponsivity (R_λ), defined as a measure of the photocurrent generated per incident light, is expressed as $I_{ph}/(P_\lambda S)$, where I_{ph} is the generated photocurrent, P_λ is the incident light power density, and S is the illuminated area.[6,38,39] The I_{ph} versus incident light power at 488 nm was measured for an InSe-FET, where the I_{ph} was observed to increase exponentially with increasing power (Figure S6, Supporting Information). In **Figure 4**a, the measured $R_{\lambda=488nm}$ values of an InSe-FET and a MoS_2/InSe-FET are plotted as a function of incident light power (0.58–2.79 μW). The InSe-FET exhibits the maximal $R_{\lambda=488nm}$ = 116 A W^{-1} (with $P_{\lambda=488nm}$ = 0.3 mW cm^{-2}),

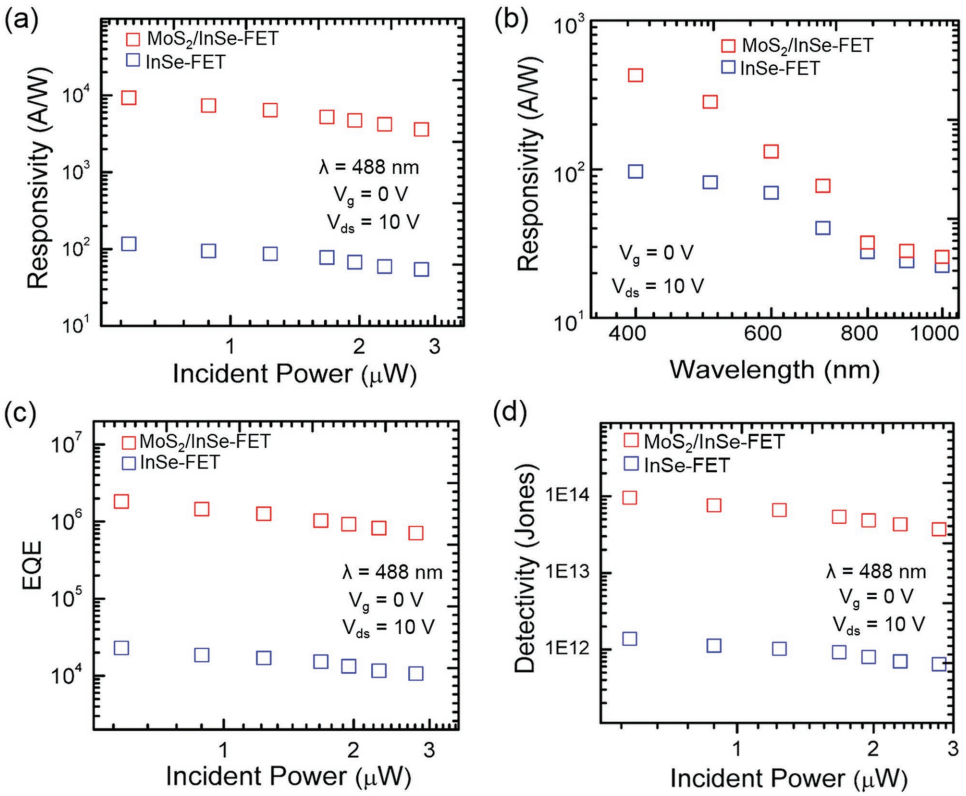

Figure 4. The photodetections of an InSe-FET and a MoS_2/InSe-FET are compared. The photoresponsivities (R_λ) were measured as a function of a) illumination power at $\lambda = 488$ nm or b) excitation wavelength. The measured c) external quantum efficiency (EQE) and d) detectivity (D^*) as a function of illumination power at $\lambda = 488$ nm are presented.

which is almost ten times higher than $R_{\lambda=450nm}$ = 12.3 A W^{-1} ($P_{\lambda=450nm}$ = 0.66 mW cm^{-2}) of our previously reported pristine InSe-FET.[28] The calculated $R_{\lambda=488nm}$ for the MoS_2/InSe-FET reaches a maximum of 9304 A W^{-1} at $P_{\lambda=488nm}$ = 0.3 mW cm^{-2} illumination, which is ≈100 times higher than the pristine InSe-FET ($R_{\lambda=488nm}$ = 116 A W^{-1} at $P_{\lambda=488nm}$ = 0.3 mW cm^{-2} excitation) without adding MoS_2 QDs in this study and several times better than other InSe-based 2D heterostructures (as listed in Table S1, Supporting Information).[27,40–42] The escalated $R_{\lambda=488nm}$ of the MoS_2/InSe-FET is due to the injection of additional photoexcited charge carriers from MoS_2 QDs to the InSe channel to enhance the photocurrent. Displayed in Figure 4b is the broadband photoresponse of our hybrid device by measuring the wavelength-dependent R_λ (λ = 400–1000 nm) at the measuring conditions of P_λ = 0.3 mW cm^{-2}, V_{ds} = 10 V, and V_g = 0 V. The bandgap of InSe nanosheets is ≈1.4 eV;[25] therefore, the spectral responsivity of the InSe-FET photodetector is active from the near-infrared to visible region (R_λ ≈ 22–96 A W^{-1}). Apparently, the hybrid MoS_2/InSe-FET has enhanced (R_λ ≈ 25–428 A W^{-1}) in the same spectral region, because of the presence of MoS_2 QDs (with a bandgap of ≈2.3 eV) to increase the visible-light absorption. The spectrum of MoS_2 QDs exhibits a strong absorption profile in the visible region (Figure S7, Supporting Information), where the generation of photoexcited carriers could be enhanced and the corresponding photoresponsivity in a MoS_2/InSe-FET could be escalated via the transfer of the photoexcited carriers to the InSe channel. In comparison, much less improvement was made in the photoresponsivity of the MoS_2/InSe-FET with the light wavelength longer than ≈800 nm, because of the weak absorption of MoS_2 QDs. This absorption profile of MoS_2 QDs reflects very closely the trend of photoresponsivity of the MoS_2/InSe-FET (Figure 4b). Table S1 in the Supporting Information compares the R_λ of a MoS_2/InSe-FET with those of the reported photodetectors fabricated with InSe heterostructures.

Next, we turn to the optoelectronic figures of merit, EQE, and specific detectivity (D^*), for the MoS_2/InSe-FET photodetector measured at 488 nm as shown in Figure 4c,d, respectively. EQE, defined as the number of electrons detected per incident photon (i.e., the net photon-to-electron conversion), is expressed as EQE = $R_\lambda \cdot [hc/(e\lambda)]$,[6,39] where R_λ is the photoresponsivity, h is Planck's constant, c is the speed of light, e is the elementary charge, and λ is the wavelength of the incident light. Figure 4c shows the EQEs of ≈10^4 and ≈10^6 for an InSe-FET and a MoS_2/InSe-FET, respectively, as a function of incident power at λ = 488 nm. Notably, the EQE of the MoS_2/InSe-FET is greater than those of the other reported hybrid photodetectors.[27,40–42] The high EQE can be accounted for by the high R_λ and large surface-to-volume ratios of the hybrid MoS_2/InSe heterostructure, of which both factors facilitate the photoabsorption of MoS_2/InSe significantly. Upon light illumination, electron–hole pairs were created by photon excitation, giving rise to the photoinduced current in photodetectors. Before the electron–hole recombination, the photoinduced

charge carriers could be trapped at the trap/defect states present at the interface of MoS_2/InSe or between the InSe channel and silicon-wafer substrate.[43,44] These captured charge carriers could prolong their lifetime, while the escaping charge carriers moved around the circuit for several times, thus enhancing EQE.[21,33] Figure S8 in the Supporting Information presents the wavelength-dependent EQEs of an InSe-FET and a MoS_2/InSe-FET measured at P_λ = 0.3 mW cm^{-2}, V_{ds} = 10 V, and V_g = 0 V.

The D^* is an indicator of the sensitivity of a photosensor and can be calculated by the relation of $D^* = R_\lambda S^{1/2}/(2eI_{dark})^{1/2}$, where R_λ, S, e, and I_{dark} are the photoresponsivity, effective area, elementary charge, and dark current, respectively.[45–47] Photosensitivity is a necessary metric, by which a photodetector can be quantified and compared with other photodetectors irrespective of the device's dimensions. The above relation can also be derived from $D^* = (S\cdot\Delta f)^{1/2}$/NEP, where S is effective area, Δf is the electrical bandwidth of a photodetector, and NEP represents the noise equivalent power, which is the measure of the weakest optical signal that a photodetector can detect.[46] Shown in Figure 4d are the calculated $D^* \geq 10^{11}$ Jones for an InSe-FET and $D^* > 10^{13}$ Jones for a hybrid MoS_2/InSe-FET (both measured at V_{ds} = 10 V and V_g = 0 V), representing the better detectivities than the commercial Si and some other 2D materials-based photodetectors (e.g., MoS_2, In_2Se_3, p-GaSe/n-InSe, and Bi_2Se_3/Si) of 10^{11}–10^{12} Jones.[41,45,47–49] The high D^* of the MoS_2/InSe-FET is attributed to the low I_{dark} of pristine (38 nA) and a hybrid MoS_2/InSe-FET (50.1 nA) along with high R_λ of this hybrid device. Time-resolved measurements were conducted for the hybrid MoS_2/InSe-FET at V_{ds} = 1 V and V_g = 0 V (Figure S9, Supporting Information). In comparison with the rising time (≈50 ms) and relaxation time (≈60 ms + 4 s) of an InSe-FET,[28] the photogenerated signal of a hybrid MoS_2/InSe-FET has slightly slower responses of ≈120 ms in rising and ≈120 ms + 5 s in relaxation. The slightly slower responses of a hybrid MoS_2/InSe-FET could be due to the presence of a few more trap states[50,51] and/or the slower charge transfer in the MoS_2/InSe interface.[52]

Next, we investigated the photovoltaic performance for the hybrid MoS_2/InSe-based device. **Figure 5**a illustrates schematically the fabricated device architecture of glass/indium tin oxide (ITO)/titanium dioxide (TiO_2)/InSe/MoS_2/Spiro ometad/Au with their corresponding energy-band alignment given in Figure 5b. It is noted that the InSe/MoS_2 heterostructure acted as an active material and the TiO_2 and Spiro ometad performed as the electrons and holes transport layers, respectively. While the TiO_2 layer was used to collect the electrons arising from the photoexcited InSe/MoS_2 heterostructure, the holes transferred to Spiro ometad and were guided to the external circuit. Figure 5c displays the photocurrent density versus voltage (J–V) curve of the hybrid MoS_2/InSe device under AM 1.5 illumination. The J–V curve of the hybrid MoS_2/InSe-based solar cell shows a typical diode behavior. The open-circuit voltage (V_{oc}) and short-circuit current density (J_{sc}) were determined to be 0.52 V and 15.6 mA cm^{-2}, respectively, yielding a photovoltaic PCE of 3.03% for the hybrid solar cell. The fill factor of ≈0.37 is excellent in comparison with the recently reported InSe-based 2D heterostructure (as listed in Table S2, Supporting Information).[40,53]

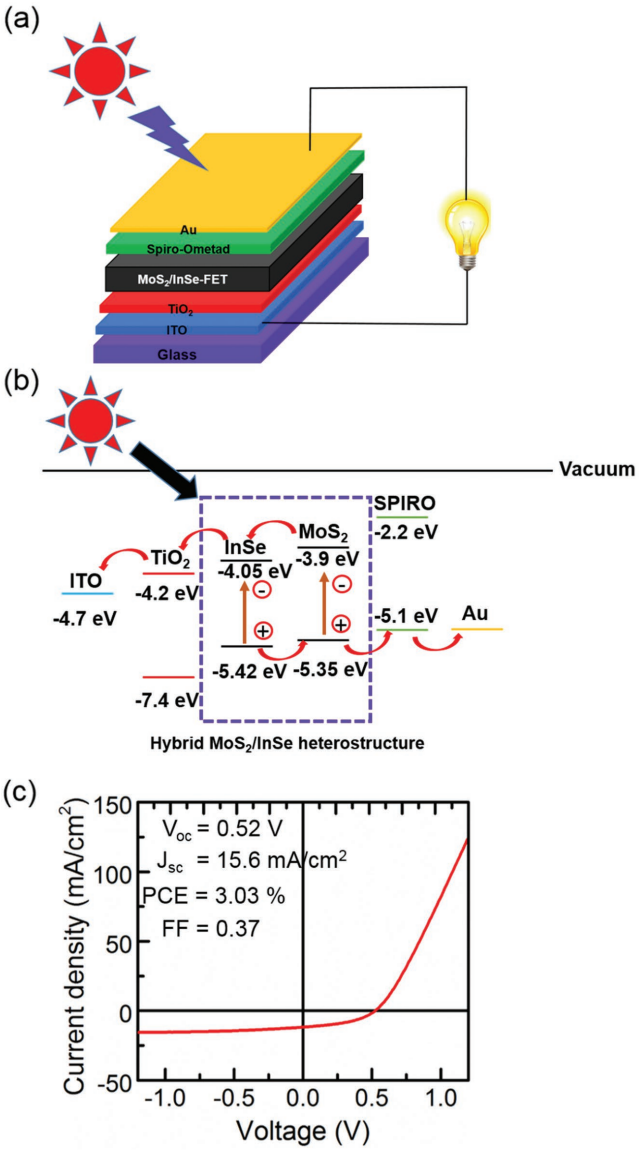

Figure 5. a) A schematic illustration for the device architecture and b) the energy-band alignment of a hybrid solar cell of glass/ITO/TiO_2/InSe/MoS_2/Spiro ometad/Au. The energy bands of the active and buffer layers are defined with respect to the vacuum. c) The J–V characteristics of the hybrid solar cell, as illustrated in a), were investigated.

3. Conclusion

In summary, we demonstrated a new hybrid optoelectronic device composed of InSe nanosheets and MoS_2 QDs. The device exhibits high $R_{\lambda=488nm} \approx 9304$ A W^{-1} with EQE ≈ 10^6 and $D^* \approx 10^{13}$ Jones. The hybrid MoS_2/InSe-FET photodetector exhibits a broadband spectral response ranging from the near-infrared (1000 nm) to visible (400 nm) region. We further showed the feasibility of using this hybrid MoS_2/InSe device toward the photovoltaic performance and determined its photovoltaic parameters of $V_{oc} \approx 0.52$ V, $J_{sc} \approx 15.6$ mA cm^{-2}, PCE ≈ 3.03%, and the fill factor of 0.37. In view of the excellent photodetection and photovoltaic characteristics with broadband

photoresponse, this hybrid MoS_2/InSe heterostructure holds great potential for high-performance optoelectronic devices in the future applications.

4. Experimental Section

Crystal Growth—InSe Crystal: The InSe single crystal was grown with the Bridgman method using the In and Se powders of 99.999% in purity (purchased from Sigma-Aldrich) as reaction precursors. The growth of InSe crystal was performed in quartz ampoules at the pressure of $\approx 7 \times 10^{-7}$ Torr. The ampoules containing the In and Se powders were heated at 850 °C for 24 h; then the ampoules were lowered through a temperature gradient of 1 °C at the rate of 0.1 mm h^{-1}. The composition ratios of the as-grown InSe single crystal were characterized to be In (51.9%) and Se (48.1%).[36]

Crystal Growth—MoS_2 Crystal: The MoS_2 single crystal was grown by chemical-vapor-transport (CVT) reaction in a three-zone horizontal furnace. The CVT system comprises a furnace with a quartz tube, closed at one end, of 100 cm in length and 12 cm/10 cm in outer/inner diameter. For the crystal growth, high-quality quartz ampoules of 32 cm in length and 2 cm/1.8 cm in outer/inner diameter were filled with ≈20 g samples containing the stoichiometric proportion (1:1) of Mo (99.999% in purity) and S (99.999% in purity) and were sealed at 10^{-5} Torr. By placing the ampoules in the three-zone horizontal furnace, the reaction and growth zones were heated slowly and later maintained at specific temperatures during the growth period.[54]

MoS_2 Quantum Dots: MoS_2 QDs were prepared from MoS_2 bulk crystal via the two successive steps of a solvothermal method. In the first step, we obtained MoS_2 nanosheets from bulk crystal by sonication. In the second step, MoS_2 QDs were obtained from the resultant MoS_2 nanosheets with a solvothermal treatment, where liquid exfoliation was performed by continuously sonicating (at 250 W) a mixture of 100 mg MoS_2 crystal and 100 mL *N*-methyl-2-pyrrolidone (NMP) in a serum bottle for 24 hr. After the liquid exfoliation, the solution was kept at room temperature for a few hours, decanted the top 2/3 of the solution into another round bottom flask, and followed by stirring and refluxing at 140 °C continuously for 12 h. Finally, the resultant mixtures were kept at room temperature for several hours and then centrifuged at 2000 rpm for 5 min to separate the supernatant from the pellets. The light yellow supernatant of MoS_2 QDs was collected for further characterizations. To remove the excessive solvent, the supernatant was evaporated under vacuum at room temperature and finally redispersed in water for further experiments.

InSe Nanosheets: The as-synthesized InSe single crystal was exfoliated into few-layered InSe nanosheets by the scotch tape-based mechanical exfoliation. The bulk crystal of InSe was placed onto an adhesive tape, followed by slightly rubbing and slicing each other for several times to yield few-layered InSe nanosheets. After the mechanical exfoliation, InSe nanosheets were transferred onto a Si wafer containing a 300 nm thick SiO_2 oxidized layer. The morphology/shape of the transferred InSe nanosheets on the Si wafer was examined using an optical microscope (Olympus, BX 51M) equipped with a charge-coupled device camera (Leica, DFC495). The thickness of InSe nanosheets was determined by AFM (Veeco, BioScope SZ).

Device Fabrication: Few-layered InSe-FETs were fabricated using a copper grid as a shadow mask to place on the exfoliated InSe nanosheets, which was assisted with a homemade micromanipulator. The source–drain electrodes of Cr/Au (5/70 nm in thickness) were deposited with a thermal evaporator.

Electron Microscopic, Optical, and Electrical Characterizations: Crystallographic phases of the as-grown crystals were examined by an X-ray diffractometer (X'Pert PRO-PANalytical, CuK_α radiation). The morphology and elemental compositions were investigated by SEM (FEI, Nova 200). TEM (JEOL, JEM-2100F) was utilized to obtain the crystalline structures and selected-area diffraction (SAED) patterns. The electrical and optical measurements at room temperature were carried out in a probe station (Lakeshore, TTPX) at 10^{-3} Torr. The probe station is equipped with a source meter (Keithley, 2636A) and an optical system comprising a He-Ne laser (JDS Uniphase, Novette 1507), a power meter (Ophir, Nova II), a xenon lamp (Newport, 66921), and a monochromator (Acton, SpectraPro-500).

Supporting Information

Supporting Information is available from the Wiley Online Library or from the author.

Acknowledgements

This work was supported, in part, by the Ministry of Science and Technology (MOST) of Taiwan under Grant Nos. 106-2627-M-002-035 and 106-2113-M-002-022-MY3.

Conflict of Interest

The authors declare no conflict of interest.

Keywords

hybrid device, nanosheets, photodetectors, photovoltaics, quantum dots

Received: September 2, 2018
Revised: October 15, 2018
Published online: November 20, 2018

[1] F. Xia, T. Mueller, Y.-M. Lin, A. V. Garcia, P. Avouris, *Nat. Nanotechnol.* **2009**, *4*, 839.
[2] F. Bonaccorso, Z. Sun, T. Hasan, A. C. Ferrari, *Nat. Photonics* **2010**, *4*, 611.
[3] Q. H. Wang, K. K. Zadeh, A. Kis, J. N. Coleman, M. S. Strano, *Nat. Nanotechnol.* **2012**, *7*, 699.
[4] K. F. Mak, C. Lee, J. Hone, J. Shan, T. F. Heinz, *Phys. Rev. Lett.* **2010**, *105*, 136805.
[5] D. Ovchinnikov, A. Allain, Y. S. Huang, D. Dumcenco, A. Kis, *ACS Nano* **2014**, *8*, 8174.
[6] P. Hu, L. Wang, M. Yoon, J. Zhang, W. Feng, X. Wang, Z. Wen, J. C. Idrobo, Y. Miyamoto, D. B. Geohegan, K. Xiao, *Nano Lett.* **2013**, *13*, 1649.
[7] M. L. Tsai, S. H. Su, J. K. Chang, D. S. Tsai, C. H. Chen, C. I. Wu, L. J. Li, L. J. Chen, J. H. He, *ACS Nano* **2014**, *8*, 8317.
[8] X. Zhang, L. Hou, A. Ciesielski, P. Samori, *Adv. Energy Mater.* **2016**, *6*, 1600671.
[9] D. Deng, K. S. Novoselov, Q. Fu, N. Zheng, Z. Tian, X. Bao, *Nat. Nanotechnol.* **2016**, *11*, 218.
[10] X. Gan, H. Zhao, X. Quan, *Biosens. Bioelectron.* **2017**, *89*, 56.
[11] X. Wang, T. Li, H. Ma, D. Zhai, C. Jiang, J. Chang, J. Wang, C. Wu, *NPG Asia Mater.* **2017**, *9*, e376.
[12] C. Biswas, Y. H. Lee, *Adv. Funct. Mater.* **2011**, *21*, 3806.
[13] F. Wang, Z. Wang, Q. Wang, F. Wang, L. Yin, K. Xu, Y. Huang, J. He, *Nanotechnology* **2015**, *26*, 292001.
[14] P. Perumal, R. K. Ulaganathan, R. Sankar, Y. M. Liao, T. M. Sun, M. W. Chu, F. C. Chou, Y. T. Chen, M. H. Shih, Y. F. Chen, *Adv. Funct. Mater.* **2016**, *26*, 3630.
[15] A. Abderrahmane, P. J. Ko, T. V. Thu, S. Ishizawan, T. Takamura, A. Sandhu, *Nanotechnology* **2014**, *25*, 365202.

[16] R. K. Ulaganathan, Y. Y. Lu, C. J. Kuo, S. R. Tamalampudi, R. Sankar, K. M. Boopathi, A. Anand, K. Yadav, R. J. Mathew, C. R. Liu, F. C. Chou, Y. T. Chen, *Nanoscale* **2016**, *8*, 2284.
[17] N. R. Pradhan, J. Ludwig, Z. Lu, D. Rhodes, M. M. Bishop, K. Thirunavukkuarasu, S. A. McGill, D. Smirnov, L. Balicas, *ACS Appl. Mater. Interfaces* **2015**, *7*, 12080.
[18] R. Frisenda, A. J. M. Mendoza, T. Mueller, A. C. Gomez, H. S. J. Van der Zant, *Chem. Soc. Rev.* **2018**, *47*, 3339.
[19] C. Chen, H. Qiao, S. Lin, C. M. Luk, Y. Liu, Z. Xu, J. Song, Y. Xue, D. Li, J. Yuan, W. Yu, C. Pan, S. P. Lau, Q. Bao, *Sci. Rep.* **2015**, *5*, 11830.
[20] A. Bablich, S. Kataria, M. C. Lemme, *Electronics* **2016**, *5*, 13.
[21] G. Konstantatos, M. Badioli, L. Gaudreau, J. Osmond, M. Bernechea, F. P. G. D. Arquer, F. Gatti, F. H. L. Koppens, *Nat. Nanotechnol.* **2012**, *7*, 363.
[22] D. Kufer, I. Nikitskiy, T. Lasanta, G. Navickaite, F. H. L. Koppens, G. Konstantatos, *Adv. Mater.* **2015**, *27*, 176.
[23] L. Gao, C. Chen, K. Zeng, C. Ge, D. Yang, H. Song, J. Tang, *Light: Sci. Appl.* **2016**, *5*, e16126.
[24] D. Kufer, T. Lasanta, M. Bernechea, F. H. L. Koppens, *ACS Photonics* **2016**, *3*, 1324.
[25] G. W. Mudd, S. A. Svatek, T. Ren, A. Patane, O. Makarovsky, L. Eaves, P. H. Beton, Z. D. Kovalyuk, G. V. lashkarev, Z. R. Kudrynskyi, A. I. Dmitriev, *Adv. Mater.* **2013**, *25*, 5714.
[26] S. Lei, F. Wen, L. Ge, S. Najmaei, A. George, Y. Gong, W. Gao, Z. Jin, B. Li, J. Lou, J. Kono, R. Vajtai, P. Ajayan, N. J. Halas, *Nano Lett.* **2015**, *15*, 3048.
[27] Z. Chen, J. Biscaras, A. Shukla, *Nanoscale* **2015**, *7*, 5981.
[28] S. R. Tamalampudi, Y. Y. Lu, R. K. Ulaganathan, R. Sankar, C. D. Liao, K. M. Boopathi, C. H. Cheng, F. C. Chou, Y. T. Chen, *Nano Lett.* **2014**, *14*, 2800.
[29] S. Xu, D. Li, P. Wu, *Adv. Funct. Mater.* **2015**, *25*, 1127.
[30] B. Radisavljevic, A. Radenovic, J. Brivio, V. Giacometti, A. Kis, *Nat. Nanotechnol.* **2011**, *6*, 147.
[31] O. L. Sanchez, D. lembke, M. Kayci, A. Radenovic, A. Kis, *Nat. Nanotechnol.* **2013**, *8*, 497.
[32] Z. Yin, H. Li, H. Li, L. Jiang, Y. Shi, Y. Sun, G. Lu, Q. Zhang, X. Chen, H. Zhang, *ACS Nano* **2012**, *6*, 74.
[33] J. Zhang, X. Y. Lang, Y. F. Zhu, Q. Jiang, *Phys. Chem. Chem. Phys.* **2018**, *20*, 17574.
[34] X. Li, J. E. Carey, J. W. Sickler, M. U. Pralle, C. Palsule, C. J. Vineis, *Opt. Express* **2012**, *20*, 5518.
[35] S. H. Yu, Y. Lee, S. K. Jang, J. Kang, J. Jeon, C. Lee, J. Y. Lee, H. Kim, E. Hwang, S. Lee, J. H. Cho, *ACS Nano* **2014**, *8*, 8285.
[36] S. Sucharitakul, N. J. Goble, U. R. Kumar, R. Sankar, Z. A. Bogorad, F. C. Chou, Y. T. Chen, X. P. A. Gao, *Nano Lett.* **2015**, *15*, 3815.
[37] J. Ali, G. U. Siddiqui, K. H. Choi, Y. Jang, K. Lee, *J. Lumin.* **2016**, *169*, 342.
[38] K. Xu, Z. Wang, F. Wang, Y. Huang, F. Wang, L. Yin, C. Jiang, J. He, *Adv. Mater.* **2015**, *27*, 7881.
[39] P. Hu, Z. Wen, L. Wang, P. Tan, K. Xiao, *ACS Nano* **2012**, *6*, 5988.
[40] W. Feng, Z. Jin, J. Yuan, J. Zhang, S. Jia, L. Dong, J. Yoon, L. Zhou, R. Vajtai, J. M. Tour, *2D Mater.* **2018**, *5*, 025008.
[41] F. Yan, L. Zhao, A. Patane, P. Hu, X. Wei, W. Luo, D. Zhang, Q. Lv, Q. Feng, C. Shen, K. Chang, L. Eaves, K. Wang, *Nanotechnology* **2017**, *28*, 27LT01.
[42] G. W. Mudd, S. A. Svatek, L. Hague, O. Makarovsky, Z. R. Kudrynskyi, C. J. Mellor, P. H. Beton, L. Eaves, K. S. Novoselov, Z. D. Kovalyuk, E. E. Vdovin, A. J. Marsden, N. R. Wilson, A. Patane, *Adv. Mater.* **2015**, *27*, 3760.
[43] M. M. Furchi, D. K. Polyushkin, A. Pospischil, T. Mueller, *Nano Lett.* **2014**, *14*, 6165.
[44] A. R. Klots, A. K. M. Newaz, B. Wang, D. Prasai, H. Krzyzanowska, J. Lin, D. Caudel, N. J. Ghimire, J. Yan, B. L. Ivanov, K. A. Velizhanin, A. Burger, D. G. Mandrus, N. H. Tolk, S. T. Pantelides, K. I. Bolotin, *Sci. Rep.* **2015**, *4*, 6608.
[45] X. Gong, M. Tong, Y. Xia, W. Cai, J. S. Moon, Y. Cao, G. Yu, C. L. Shieh, B. Nilsson, A. J. Heeger, *Science* **2009**, *325*, 1665.
[46] M. Buscema, J. O. Island, D. J. Groenendijk, S. I. Blanter, G. A. Steele, H. S. J. van der Zant, A. C. Gomez, *Chem. Soc. Rev.* **2015**, *44*, 3691.
[47] R. B. J. Gedrim, M. Shanmugam, N. Jain, C. A. Durcan, M. T. Murphy, T. M. Murray, R. J. Matyi, R. L. Moore, B. Yu, *ACS Nano* **2014**, *8*, 514.
[48] H. Zhang, X. Zhang, C. Liu, S. T. Lee, J. Jie, *ACS Nano* **2016**, *10*, 5113.
[49] W. Choi, M. Y. Cho, A. Konar, J. H. Lee, G. B. Cha, S. C. Hong, S. Kim, J. Kim, D. Jena, J. Joo, S. Kim, *Adv. Mater.* **2012**, *24*, 5832.
[50] J. Schornbaum, B. Winter, S. P. Schie, F. Gannott, G. Katsukis, D. M. Guldi, E. Spiecker, J. Zaumseil, *Adv. Funct. Mater.* **2014**, *24*, 5798.
[51] Z. Jia, J. Xiang, C. Mu, F. Wen, R. Yang, C. Hao, Z. Liu, *J. Mater. Sci.* **2017**, *52*, 11506.
[52] Z. Jia, J. Xiang, F. Wen, R. Yang, C. Hao, Z. Liu, *ACS Appl. Mater. Interfaces* **2016**, *8*, 4781.
[53] W. Feng, W. Zheng, X. S. Chen, G. Liu, W. Cao, P. Hu, *Chem. Mater.* **2015**, *27*, 983.
[54] J. Suh, T. L. Tan, W. Zhao, J. Park, D.-Y. Lin, T.-E. Park, J. Kim, C. Jin, N. Saigal, S. Ghosh, Z. M. Wong, Y. Chen, F. Wang, W. Walukiewicz, G. Eda, J. Wu, *Nat. Commun.* **2018**, *9*, 199.

